Carbon 139 (2018) 145–155

Contents lists available at ScienceDirect

Carbon

journal homepage: www.elsevier.com/locate/carbon

# $MnO_2$ nanoparticles anchored on carbon nanotubes with hybrid supercapacitor-battery behavior for ultrafast lithium storage

Datao Wang [a], Ke Wang [b], Li Sun [b], Hengcai Wu [a], Jing Wang [a], Yuxing Zhao [a], Lingjia Yan [a], Yufeng Luo [a], Kaili Jiang [a, c], Qunqing Li [a, c], Shoushan Fan [a], Ju Li [d], Jiaping Wang [a, c, d, *]

[a] Department of Physics and Tsinghua-Foxconn Nanotechnology Research Center, Tsinghua University, Beijing, PR China
[b] School of Materials Science and Technology, China University of Geosciences, Beijing, PR China
[c] Collaborative Innovation Center of Quantum Matter, Beijing, PR China
[d] Department of Nuclear Science and Engineering and Department of Materials Science and Engineering, Massachusetts Institute of Technology, Cambridge, USA

ARTICLE INFO

*Article history:*
Received 11 April 2018
Received in revised form
16 June 2018
Accepted 20 June 2018
Available online 21 June 2018

ABSTRACT

Developing hybrid supercapacitor-battery energy storage devices for applications in electric vehicles is attractive because of their high energy density and short charge/discharge time. In this study, flexible $MnO_2$ nanoparticle-coated air-oxidized carbon nanotube ($MnO_2$/aCNT) electrodes are fabricated by the in situ redox reaction of $KMnO_4$ and aCNTs at room temperature. The $MnO_2$ nanoparticles have diameters of ~10 nm. There is a strong chemical interaction between the $MnO_2$ active material and aCNTs as a result of the Mn–O–C linkage. The flexible aCNT network can alleviate the strain from the $MnO_2$ volume change and maintain the electrode integrity during rapid charge/discharge. The aCNT framework also provides a continuous and rapid electron pathway and ensures uniform dispersion of the $MnO_2$ nanoparticles. The presence of $MnO_2$ nanoparticles provides short pathways for Li-ion diffusion and allows interfacial capacitive lithium storage for ultrafast and reversible lithium storage. We report the best high-current performance to date for $MnO_2$/C electrodes, of 395.8 mA h $g^{-1}$ at 10 A $g^{-1}$, and 630.2 mA h $g^{-1}$ after 150 cycles at 2 A $g^{-1}$. The excellent electrochemical performance, combined with the capacitive dominating process of the electrode, will further the design of high-performance hybrid supercapacitor-battery energy storage devices.



## 1. Introduction

Rechargeable energy storage devices (e.g. lithium-ion batteries and supercapacitors) are attractive for applications in portable electronics and electric vehicles. Such technologies will help to meet increasing demands for environmentally friendly energy devices. Lithium-ion (Li-ion) batteries typically provide a high energy density of 150–200 W h $kg^{-1}$, which is achieved through lithium insertion and extraction reactions at a high cell voltage ($\geq$ 3V). However, the power performance of Li-ion batteries ($\ll$1 kW $kg^{-1}$) remains far below theoretically predicted levels [1]. Practical applications such as transportation and grid storage require the rapid delivery or receiving of large amounts of energy on the timescale of seconds. Electrochemical supercapacitors can achieve a high power density (>10 kW $kg^{-1}$). They do so through adsorbing ions onto the electrode/electrolyte interface to act as electrical double-layer capacitors and also by exploiting fast faradic surface redox reactions to act as pseudocapacitors [2]. However, supercapacitors are limited by their low energy density (<10 W h $kg^{-1}$), because charge is confined to the surface. It is desirable to develop an electrochemical energy storage device that combines the advantages of the high energy density of batteries and the high power density of supercapacitors [3].

Nanostructured transition metal oxides such as $Co_3O_4$, $TiO_2$, $Fe_3O_4$, MnO, $MnO_2$, and $Mn_3O_4$ have been intensively studied as electrode materials in Li-ion batteries. They can potentially provide a high power density, because of their capacitive lithium storage behavior and high theoretical capacitance [4–12]. The application

* Corresponding author. Department of Physics and Tsinghua-Foxconn Nanotechnology Research Center, Tsinghua University, Beijing, 100084, PR China.
*E-mail address:* jpwang@tsinghua.edu.cn (J. Wang).

https://doi.org/10.1016/j.carbon.2018.06.046
0008-6223/

of transition metal oxides for high energy density at high rates is currently limited by their poor electronic conductivity, low Li-ion ($Li^+$) diffusion coefficient, slow reaction kinetics, and poor structural stability during cycling. A strategy for overcoming these challenges is to design nanoparticles that combine rapid surface redox processes and solid-state lithium diffusion to deliver high power densities [3,13,14]. Nanostructured active materials have advantages for realizing high-power Li-ion batteries [13,15–18]. First, the nanostructure provides short $Li^+$ diffusion pathways, which provide fast diffusion kinetics and thus enhance current-rate capability. Second, the large surface area of the nanoparticles enables the electrode to accommodate the strain and mechanically buffer the volume change during the charge/discharge process, thus maintaining the electrode integrity and promoting cycling stability. Many nanostructured transition metal oxides and porous materials have been fabricated and investigated as advanced energy storage devices, which exhibit the behavior of both supercapacitors and batteries. These include $\gamma$-$Fe_2O_3$, $V_2O_5$/carbon nanotubes (CNTs), MnO/reduced graphene oxide (rGO), and metal-organic frameworks [15,19–21]. However, there are two major problems for the electrodes containing nanostructured active materials. First, nanoparticles often aggregate into larger particles that have limited contact with conductive additives and current collectors. This prevents full utilization of the active material during cycling [22]. It is important to develop conductive frameworks in which nanostructured active materials can be uniformly loaded. The conductive frameworks should provide three-dimensional (3D) electron and ion transport pathways for the active materials [23]. Second, many binders cannot accommodate the strain of electrodes generated at ultrahigh current densities. This is a result of the weak van der Waals interactions between the binders and active particles, which can result in electrode fracture and pronounced capacity fade [24,25]. A strong chemical interaction between the active materials and conductive framework is important for providing robust mechanical adhesion, and thus improving the rate capability and cycling life [26].

Super-aligned CNTs (SACNTs) possess a large aspect ratio ($>10^4$), clean surface, high conductivity, good mechanical strength, and flexibility. SACNTs can be assembled into a continuous conductive framework to fabricate free-standing composite electrodes with transition metal oxides such as $Co_3O_4$, $Mn_3O_4$, and $Fe_3O_4$ [27–30]. $MnO_2$ is a widely used pseudocapacitive material that shows great promise in simultaneously achieving high-energy and high-power performance [31]. The advantages of $MnO_2$ include a high theoretical capacity (1233 mA h $g^{-1}$), natural abundance, and environmental benignity. The application of $MnO_2$ is limited by its intrinsic low electrical conductivity and mechanical instability [8].

In the current study, a strategy based on the redox reaction of $KMnO_4$ and air-oxidized SACNTs (aCNTs) is used to synthesize $MnO_2$ nanoparticles anchored on aCNTs. The resulting $MnO_2$/aCNT electrodes exhibit excellent high-rate performance. The nanostructured $MnO_2$ particles with diameters of approximately 10 nm provide a short $Li^+$ diffusion path length, and allow rapid capacitive-controlled lithium storage. The 3D aCNT matrix serves as a supporting framework, providing continuous electron pathways for the $MnO_2$ nanoparticles. There is a strong chemical interaction between the $MnO_2$ particles and aCNT framework, as a result of the Mn–O–C linkage. This strong interaction ensures that the $MnO_2$ particles are strongly attached to the aCNTs, which promotes mechanical stability and maintains the electrode integrity during cycling. These features in the free-standing $MnO_2$/aCNT electrodes lead to favorable lithium pseudocapacitance with high-rate capability. These findings will promote the development of hybrid supercapacitor-battery energy storage devices.

## 2. Experimental

### 2.1. Fabrication of CNTs

SACNT arrays with a CNT diameter of 20–30 nm and an array height of 300 μm were synthesized by low-pressure chemical vapor deposition (LP-CVD), wherein iron was used as the catalyst and acetylene as the precursor. Details of the synthetic process can be found in previous papers [27]. The pristine SACNTs were heated to 550 °C in air at a rate of 15 °C $min^{-1}$, and then held at 550 °C for 30 min to introduce negatively charged oxygenated functional groups [32]. The resulting air-oxidized SACNTS are hereafter referred to as aCNTs. Pristine SACNTs (pCNTs) and commercially available randomly oriented multi-walled CNTs (rCNTs, with diameters of 20–50 nm, Shenzhen Nanotech Port Co., P. R. China) were used to prepare comparative samples.

### 2.2. Fabrication of $MnO_2$/aCNT electrodes

$MnO_2$/aCNT nanocomposites were synthesized by the redox reaction of $KMnO_4$ and aCNTs. 100 mg of aCNTs or pCNTs were dispersed in deionized water via ultrasonication, which disrupted their super-aligned structures. 1.0 g of $KMnO_4$ was added to the suspension under mixing, which was then magnetically stirred for 3 days at 25 °C. After collection by filtration and drying in an oven at 120 °C, a free-standing $MnO_2$/aCNT or $MnO_2$/pCNT electrode was obtained. No additional current collectors or binders were introduced. The $MnO_2$ loading and content in the composite were 1.5 mg $cm^{-2}$ and 50 wt%, respectively. The thickness and area of the electrode were 100 μm and 0.6–0.8 $cm^2$, respectively. The tap density of the electrode was 0.3 g $cm^{-3}$. An aCNT electrode without $MnO_2$ was also prepared for comparison, using the same filtration and drying method. pCNTs or rCNTs were also treated with $KMnO_4$ to prepare $MnO_2$/pCNT or $MnO_2$/rCNT electrode with a 50 wt% $MnO_2$ loading. The rCNTs and $MnO_2$ particles could not form a self-supporting composite electrode in the absence of adhesives. Thus, the rCNTs loaded with $MnO_2$ particles were mixed with carbon black (Super-P, 50 nm particle diameter, Timcal Ltd., Switzerland) and poly(vinylidene difluoride) (PVDF) in N-methyl-2-pyrrolidone (NMP) solvent. The resulting mixture was then coated onto a Cu current collector. $MnO_2$ electrodes containing $MnO_2$, Super-P, and PVDF at a weight ratio of 5:4:1 were also prepared using the same casting method.

### 2.3. Characterization

The morphologies of the $MnO_2$/CNT electrodes were characterized using scanning electron microscopy (SEM; Sirion 200, FEI) and transmission electron microscopy (TEM; Tecnai G2F20, FEI). The $MnO_2$ contents in the nanocomposites were determined using thermogravimetric analysis (TGA; PerkinElmer, USA) at a heating rate of 10 °C $min^{-1}$. Raman spectra of the $MnO_2$ powder, aCNTs, $MnO_2$/aCNT, $MnO_2$/pCNT, and $MnO_2$/rCNT composites were recorded using a Horiba spectrometer (514 nm Ar laser, 24 mW). X-ray photoelectron spectra (XPS) of the $MnO_2$ powder, aCNTs, and $MnO_2$/aCNT composites were recorded using a PHI Quantera II surface analysis equipment. X-ray diffraction (XRD) patterns of the $MnO_2$/aCNT composites were collected using an X-ray diffractometer (Rigaku, Cu Kα radiation) at a scan rate of 2° $min^{-1}$. A surface area and porosity analyzer (ASAP 2020 HD88, BET) was used to measure the specific surface area and pore size distribution of the pCNTs, aCNTs, and $MnO_2$/aCNT composites.

Coin-type (CR 2016) half-cells were assembled in an Ar-filled glove box, using the above-prepared nanocomposites as the working electrode and lithium foil as the counter electrode. A

polypropylene film (Celgard 2400) was used as the separator. The electrolyte was 1 M $LiPF_6$, with an ethylene carbonate (EC): diethyl carbonate (DEC) weight ratio of 1:1. Galvanostatic charge-discharge tests were carried out using a Land battery test system (Wuhan Land Electronic Co., P. R. China) with cut-off voltages of 0.01–3.0 V. Cyclic voltammetry (CV) and electrochemical impedance spectroscopy (EIS) measurements were carried out using a Galvanostat instrument (EG&G Princeton Applied Research 273A).

## 3. Results and discussion

Fig. 1a shows a schematic of the strategy to fabricate the free-standing $MnO_2$/aCNT electrodes. TEM images of the pCNTs, aCNTs, and $MnO_2$ nanoparticles on aCNTs are shown in Fig. 1b, c, and d, respectively. These images show the morphological changes that occurred during the fabrication process. The pristine SACNT array was heated in air, and thus aCNTs were obtained with etching defects on the tube walls as indicated by the red arrow in Fig. 1c. aCNTs were dispersed in deionized water via a sonication-assisted method as reported previously [33]. When the $KMnO_4$ solution was mixed with the aqueous aCNT dispersion at room temperature, $KMnO_4$ was gradually reduced by aCNTs according to $4MnO_4^- + 3C + H_2O \rightarrow 4MnO_2 + CO_3^{2-} + 2HCO_3^-$ [8,34]. During the slow redox process, $MnO_2$ particles with an average diameter of 10 nm either anchored on the aCNT surface or were encapsulated between adjacent aCNTs (Figure S1 a) (Please change to Fig. S1 a). $MnO_2$ nanoparticle agglomeration was not observed outside of the aCNT bundles. The nanosized $MnO_2$ particles provided a large fraction of surface atoms to directly contact with the electrolyte, which provided short $Li^+$ diffusion pathways and thus allowed for rapid $Li^+$ transport. The flexible aCNT network served as a conductive bridge between the insulating $MnO_2$ nanoparticles and maintained the stability of the electrode structure.

Nanoparticles on the aCNTs were identified as δ-$MnO_2$ by the XRD pattern (Fig. 2a). The strong XRD peak at around 26° was attributed to the (002) crystal plane of the graphite lattice in the aCNTs [29]. Other XRD peaks were consistent with those of the birnessite-type δ-$MnO_2$ phase (JCPDS No. 80–1098). An interplanar $d_{100}$ spacing of 0.25 nm was observed from a high-resolution TEM image of the $MnO_2$ nanocrystals (Fig. 2a inset), which was also consistent with literature values for monoclinic birnessite-type δ-$MnO_2$ [35,36].

The hybridization changes and structural information in the $MnO_2$/aCNT composites were investigated by Raman spectroscopy. Fig. 2b shows peaks at 1348 $cm^{-1}$ (D band, defects or structural disorder) and 1582 $cm^{-1}$ (G band, $sp^2$ carbon domains) in the Raman spectra of the aCNTs and $MnO_2$/aCNT composites. These results indicated that the structure of the aCNTs was maintained

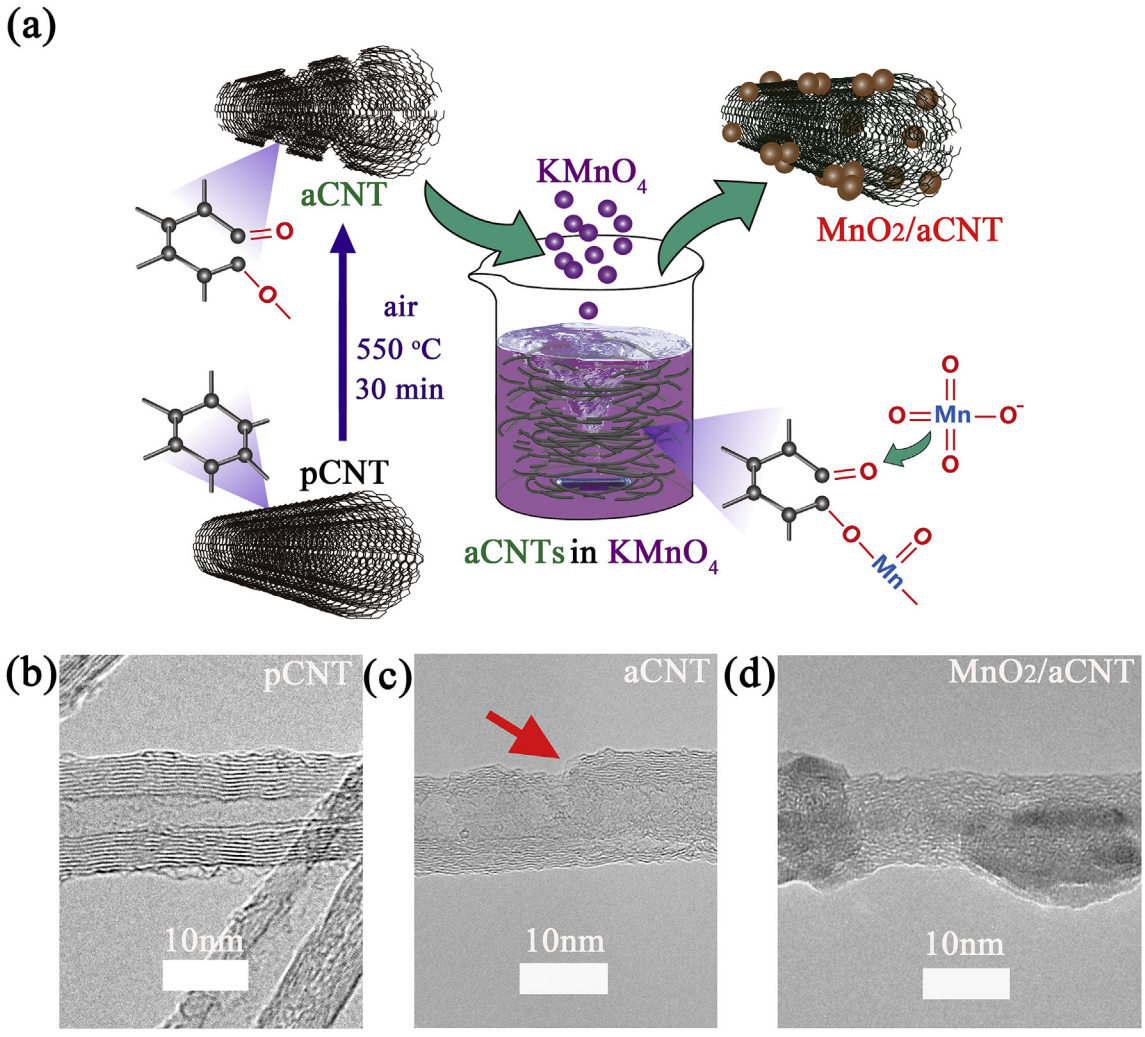


**Fig. 1.** (a) Schematic of the process for fabricating the $MnO_2$/aCNT electrode. TEM images of (b) pCNTs, (c) aCNTs, and (d) $MnO_2$ nanoparticles on aCNTs. (A colour version of this figure can be viewed online.)

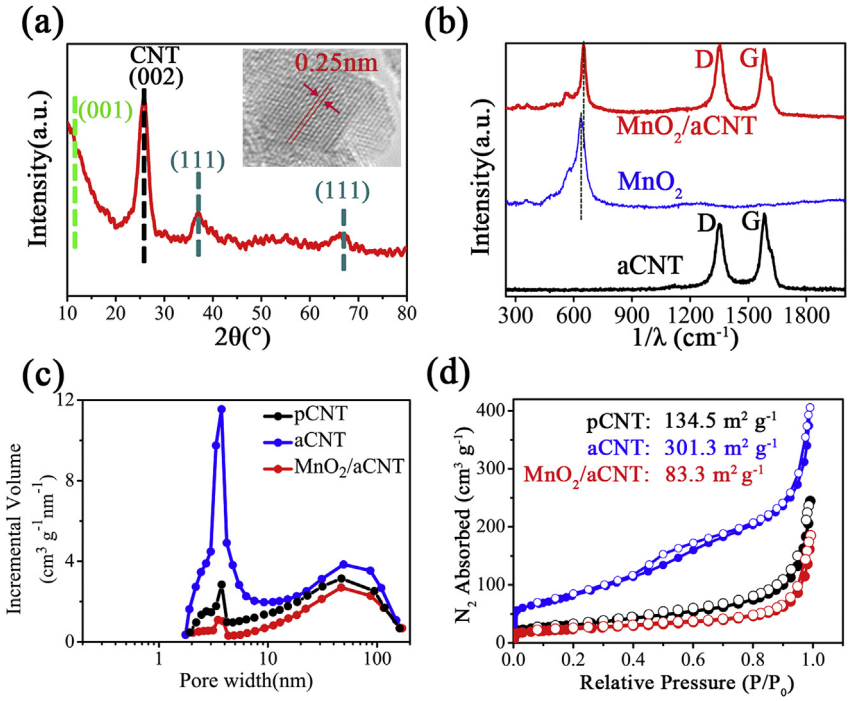


**Fig. 2.** (a) XRD pattern of the $MnO_2$/aCNT composite. Inset: High-resolution TEM image of $MnO_2$ nanocrystals. (b) Raman spectra of the aCNTs, $MnO_2$ powder, and $MnO_2$/aCNT composites. (c) Pore size distributions and (d) nitrogen adsorption-desorption isotherms of the pCNTs, aCNTs, and $MnO_2$/aCNT composite. (A colour version of this figure can be viewed online.)

during the redox reaction. The increased intensity ratio of the D band to G band ($I_D/I_G$) in the Raman spectrum of the $MnO_2$/aCNT composites compared to the aCNTs suggested a higher defect concentration due to the oxidation by $KMnO_4$. The Raman peaks at 560–570 $cm^{-1}$ (Fig. 2b) in the spectra of the $MnO_2$ powder and $MnO_2$/aCNT composites were attributed to the $\upsilon_3$ (Mn–O) stretching vibration with $F_{2g}$ symmetry, owing to the presence of $Mn^{4+}$. The Raman peaks at 634 $cm^{-1}$ ($MnO_2$) and 650 $cm^{-1}$ ($MnO_2$/aCNT composites) were related to the $\upsilon_2$ (Mn–O) symmetric stretching vibrations of the [$MnO_6$] octahedron [37]. There was a slight frequency difference between these peaks in the spectra of $MnO_2$ and the $MnO_2$/aCNT composites. This correlated to the shorter Mn–O bonds in the $MnO_2$/aCNT composites, owing to the local lattice distortion by incorporating $K^+$ into the interlayer space [38].

$N_2$ adsorption/desorption experiments were conducted to investigate the microstructures of the pCNTs, aCNTs, and $MnO_2$/aCNT composites. Pore size distributions and isotherm loops are shown in Fig. 2c and d, respectively. The specific surface areas were 134.5 $m^2 g^{-1}$, 301.3 $m^2 g^{-1}$, and 83.3 $m^2 g^{-1}$ for the pCNTs, aCNTs, and $MnO_2$/aCNT composites, respectively, as calculated from the isotherm loops. For the pCNTs, the two peaks at 3–5 nm and 40–70 nm in the pore size distribution were assigned to the internal diameter of the nanotubes and pores between neighboring bundles, respectively. In comparison with the pristine CNTs, the aCNTs possessed a much higher specific surface area (2.24 times that of the pCNTs), and a more pronounced pore peak at 3–5 nm. These observations corresponded to the increased surface area resulting from the oxidation defects on the tube walls. The profiles of the isotherms of the pCNTs and aCNTs differed in the $P/P_0$ range of 0.4–1.0 (Fig. 2d). This further confirmed that extra pores were created during the air oxidation process. After the redox reaction between $KMnO_4$ and the aCNTs, $MnO_2$ nanoparticles anchored on the aCNTs. The specific surface area decreased to 83.3 $m^2 g^{-1}$s, and pores of 3.7 nm in diameter became almost absent. This corresponded to the encapsulation of $MnO_2$ nanoparticles in the abundant mesopores on the aCNT surface. The similar isotherm profiles of the pCNTs and $MnO_2$/aCNT composites indicated their same mesoporous structures. This implied that the $MnO_2$ nanoparticles preferred to reside in the mesopores introduced into the aCNTs during the air oxidation process. The above results were consistent with the TEM observations of the $MnO_2$/aCNT composites.

The $MnO_2$ electrodes, $MnO_2$/rCNT electrodes, and $MnO_2$/pCNT electrodes were also fabricated and investigated for comparison. Fig. 3a–d show SEM images of the $MnO_2$, $MnO_2$/rCNT, $MnO_2$/pCNT, and $MnO_2$/aCNT electrodes, respectively. The aggregation of both carbon black and $MnO_2$ particles was apparent in the $MnO_2$ electrode, and the $MnO_2$ nanoflakes tended to aggregate into spheres (Fig. 3a). Introducing rCNTs did not lead to any obvious improvement to the dispersion of $MnO_2$ particles in the $MnO_2$/rCNT electrode compared to the $MnO_2$ electrode (Fig. 3b). Both $MnO_2$/pCNT (Fig. 3c) and $MnO_2$/aCNT electrode (Fig. 3d) demonstrated 3D continuous scaffold structures, and the $MnO_2$/aCNT electrode exhibited smaller CNT bundles without any $MnO_2$ aggregation. TEM observations further showed the details of the morphological difference between the $MnO_2$/CNT electrodes (Fig. S1): Both $MnO_2$/aCNT (Figure S1 a) and $MnO_2$/pCNT (Fig. S1b) electrodes consisted of $MnO_2$ nanoparticles uniformly anchored on the surface of the CNTs, but a small part of $MnO_2$ nanoparticles still agglomerated in the $MnO_2$/pCNT electrode. In comparison, most $MnO_2$ particles and rCNTs aggregated into spheres in the $MnO_2$/rCNT electrode (Fig. S1c). TGA measurements were carried out to evaluate the contents of $MnO_2$, CNTs, and interlayer water in the $MnO_2$/CNT electrodes (Fig. S1d). The weight losses occurring in the temperature ranges of <100 °C, 100–300 °C and >600 °C corresponded to 1.5–2.5 wt% physically adsorbed water, 6 wt% chemisorbed structural water and ~50 wt% of $MnO_2$ in all the $MnO_2$/CNT composites.

The different morphologies of the $MnO_2$/rCNT, $MnO_2$/pCNT, and $MnO_2$/aCNT can be ascribed to their corresponding CNT dispersion

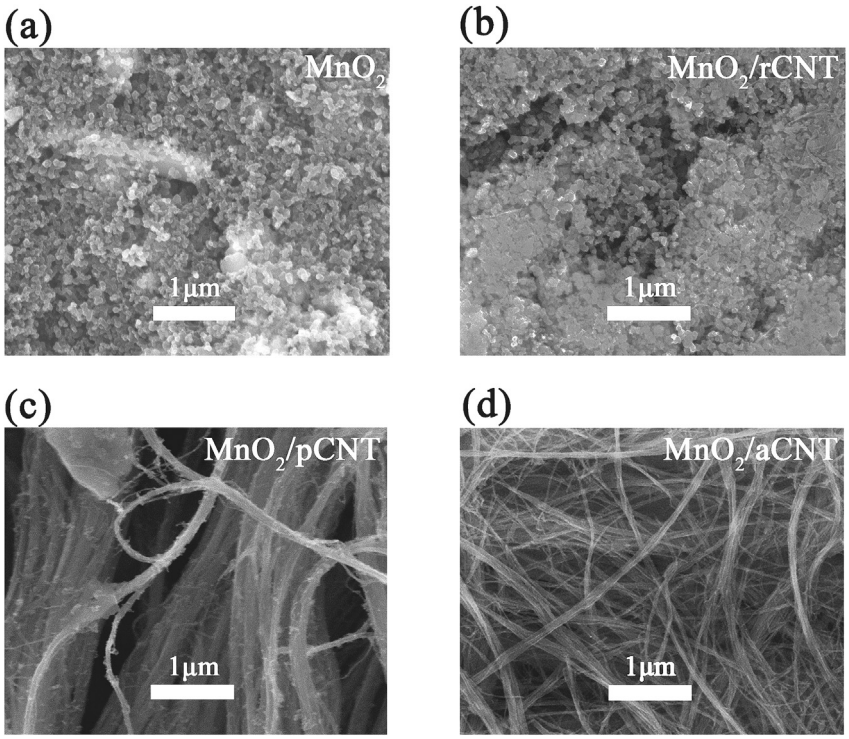


**Fig. 3.** SEM images of the (a) $MnO_2$, (b) $MnO_2$/rCNT, (c) $MnO_2$/pCNT, and (d) $MnO_2$/aCNT electrodes.

behaviors. Fig. S2 shows SEM and TEM images of rCNTs, pCNTs, and aCNTs. The highly agglomerated and entangled rCNTs could not form a continuous scaffold (Figs. S2a and S2b) [39]. Both binders and current collectors were required to obtain $MnO_2$/rCNT electrodes. In contrast, the agglomeration problem was mitigated for both pCNTs and aCNTs due to their super-aligned nature during the synthesis process [27], and thus they were able to assemble and interweave into continuous 3D mats (Figs. S2c–f). The CNT mats served as self-supporting frameworks, enabling the formation of freestanding electrodes based on CNTs. Figs. S3a and b showed digital photographs of a flexible and freestanding aCNT film and a $MnO_2$/aCNT electrode, respectively. Note that pCNT films and $MnO_2$/pCNT electrodes demonstrated similar flexibility as aCNT films and $MnO_2$/aCNT electrodes.

XPS spectra of pCNTs, aCNTs, rCNTs, and their corresponding $MnO_2$/CNT composites were performed to characterize the chemical interactions. The XPS spectra of the aCNTs (Fig. 4a) were divided into four components at 284.8 eV, 285.7 eV, 287 eV and 291.2 eV, corresponding to $sp^2$ carbon, $sp^3$ carbon, carbon in C–O/C=O groups, and $\pi$-$\pi^*$ transition, respectively. The C 1s spectra of the rCNTs (Fig. S4a) and pCNTs (Fig. S5a) demonstrated similar patterns of $sp^2$ carbons, $sp^3$ carbons, and $\pi$-$\pi^*$ transition, but without any oxygen-containing moieties. Compared to rCNTs, pCNTs, and aCNTs, the C 1s spectra of the $MnO_2$/rCNT (Fig. S4b), $MnO_2$/pCNT (Fig. S5b) and $MnO_2$/aCNT (Fig. 4b) electrodes exhibited higher C–O/C=O peak binding energy and higher amount of oxygenated functional groups, as a result of oxidation of the CNTs by $KMnO_4$. The presence of $K^+$ in all the $MnO_2$/CNT composites was confirmed by peaks at 292.9±0.1 eV and 295.5 eV related to the K $2p_{3/2}$ and K $2p_{1/2}$ states in the XPS spectra, respectively (Figs. 4b, S4b, and S5b) [40]. Fig. 4c, Fig. S4c, and Fig. S5c show the core level binding energies for the Mn 2p peaks in the $MnO_2$/aCNT, $MnO_2$/rCNT, and $MnO_2$/pCNT composites, respectively. The binding energies for the Mn $2p_{3/2}$ and Mn $2p_{1/2}$ states were observed at 642.0 eV and 653.5 eV, respectively, which were similar to those reported for the $Mn^{4+}$ oxidation state [8,37].

The XPS spectra of the O 1s region for the aCNTs, $MnO_2$ powder, and $MnO_2$/aCNT composites are shown in Fig. 4d–f, respectively. In the spectrum of the aCNTs, the peaks at 530.8 eV and 532.2 eV were ascribed to the C=O and C–O bonds, respectively (Fig. 4d). The peak at 529.6 eV in the spectrum of the $MnO_2$ powder was assigned to the Mn–O bonding in [$MnO_6$] octahedra, and the peaks at 530.8 eV and 532.2 eV originated from hydroxide and waters of crystallization (Fig. 4e). The O 1s spectrum of the $MnO_2$/aCNT composites in Fig. 4f was deconvoluted into four peaks at 529.6 eV, 530.8 eV, 531.5 eV, and 532.2 eV, which corresponded to the O 1s states of oxide (Mn–O–Mn), hydroxide (Mn–O–H)/C=O bonds, Mn–O–C linkages, and interlayer water (H–O–H)/C–O bond, respectively [41,42]. Compared with the O 1s spectra of the $MnO_2$ powder and aCNTs, the extra peak at 531.5 eV indicated the formation of Mn–O–C bridges at the $MnO_2$/aCNT interface. The Mn–O–C linkage may have originated from an anion adsorption mechanism, in which oxygen-containing groups on the carbon template captured metal anions (such as $VO_3^-$, $MnO_4^-$, and $MoO_4^-$) [43]. According to this mechanism, $MnO_4^-$ groups were adsorbed by the C–O/C=O groups on the aCNTs. The presence of the Mn–O–C linkage further confirmed that the $MnO_2$ nanoparticles and aCNTs were chemically hybridized with each other. This strong chemical connection can prevent detachment of the active $MnO_2$ nanoparticles from the aCNTs during rapid cycling. In contrast, neither $MnO_2$/rCNT nor $MnO_2$/pCNT electrodes demonstrated the Mn–O–C linkage in the O 1s XPS spectra (Figs. S4d and S5d), because both rCNTs and pCNTs did not possess oxygen-containing groups and were unable to capture metal anions during the oxidation process by $KMnO_4$. Therefore, $MnO_2$ nanoparticles tended to aggregate (Figs. S1b and c) instead of closely anchoring on the CNTs due to the absence of the Mn–O–C linkage.

The morphology and structure of $MnO_2$ was expected to affect the degree of polarization and reversibility of the electrodes during cycling. Fig. 5a–d shows discharge curves of the $MnO_2$, $MnO_2$/rCNT,

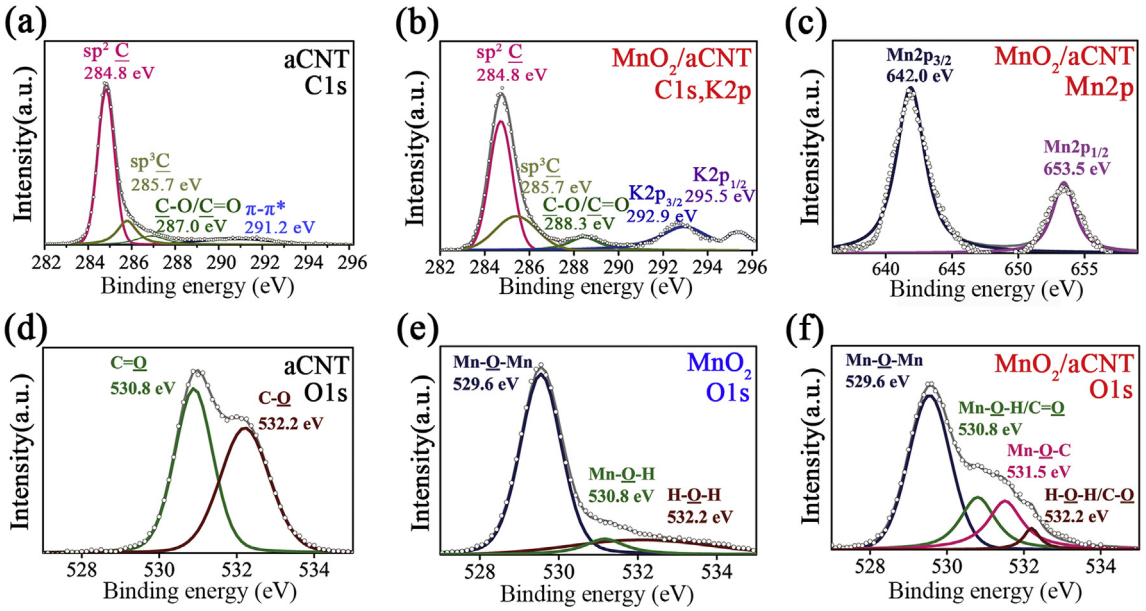


**Fig. 4.** XPS spectra: (a) C1s region for the aCNTs. (b) C1s and K2p, (c) Mn2p regions for the $MnO_2$/aCNT composite. O1s region for the (d) aCNTs, (e) $MnO_2$ powder, and (f) $MnO_2$/aCNT composite. (A colour version of this figure can be viewed online.)

$MnO_2$/pCNT, and $MnO_2$/aCNT electrodes at 0.2 A $g^{-1}$, respectively. The discharge curves of the four electrodes shared common characteristics. Specifically, a slope region from 3.0 V to 0.5 V and a plateau at 0.4–0.5 V were assigned to the reduction of $MnO_2$ to Mn(II) and the further reduction of Mn(II) to Mn(0), respectively. The irreversible capacity loss in the first cycle was attributed to the formation of a solid electrolyte interphase (SEI) film. The profile of the $MnO_2$/pCNT and $MnO_2$/aCNT electrodes exhibited three features that differed to the $MnO_2$ and $MnO_2$/rCNT electrodes: (1) Both $MnO_2$/pCNT and $MnO_2$/aCNT electrodes retained approximately 70% of the initial capacity from the first cycle to the second cycle, which suggested better reversibility than the other two electrodes. The lower irreversible capacity loss in the first cycle may have arisen from the reduced SEI formation time. This reduced formation time arose from the superior wettability of the oxygenated functional groups in the composites and also from the smooth electrode surface. In the $MnO_2$ and $MnO_2$/rCNT electrodes, the presence of inactive binders, conductive additives, and rough electrode surfaces may have hindered SEI formation, resulting in larger initial irreversible capacity losses [44]. (2) The small voltage drop $\Delta U$ of the $MnO_2$/pCNT electrode and $MnO_2$/aCNT electrode ($\Delta U_{1st} = 0\,V$, $\Delta U_{2nd} < 0.25\,V$, $\Delta U_{50th} < 0.10\,V$) when charging was switched to

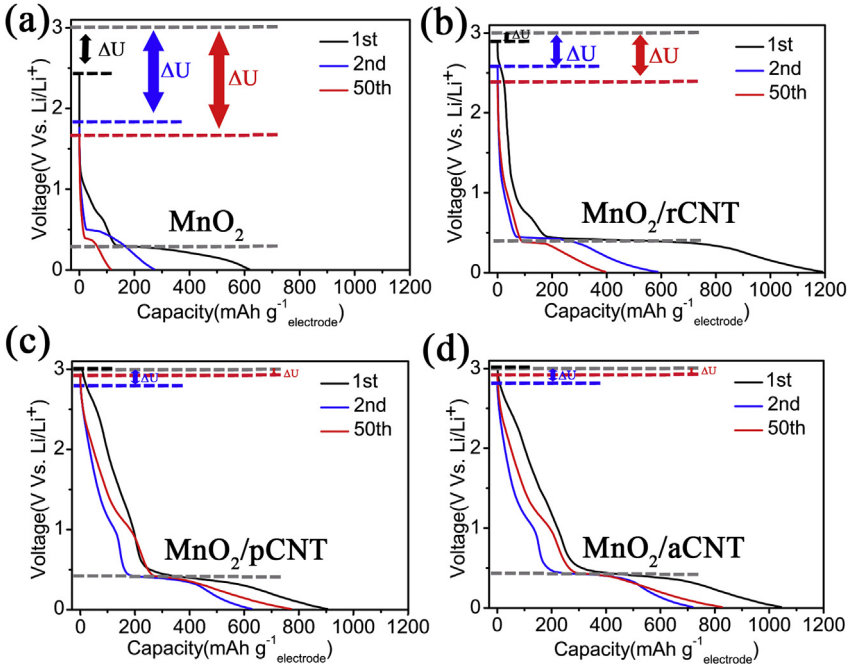


**Fig. 5.** Discharge curves of the (a) $MnO_2$, (b) $MnO_2$/rCNT, (c) $MnO_2$/pCNT, and (d) $MnO_2$/aCNT electrodes in the 1st, 2nd, and 50th cycles at 0.2 A $g^{-1}$. (A colour version of this figure can be viewed online.)

discharging reflected a low contact resistance and inhibition of polarization. These factors reflected the relatively homogenous dispersion of $MnO_2$ nanoparticles on the CNT framework. The agglomeration of $MnO_2$ particles in the $MnO_2$ and $MnO_2$/rCNT electrodes led to severe polarization and relatively high voltage drops. (3) From the 2nd cycle to the 50th cycle, both the $MnO_2$/pCNT and $MnO_2$/aCNT electrodes exhibited slight capacity increase, while the other two electrodes exhibited capacity fading. In general, during the initial wetting and activation process, electrodes exhibit capacity increase until full wetting of the electrode and full utilization of the active material. The irreversible capacity loss and reversibility of the electrode reportedly affect the capacity fading rate [44,45]. The high reversibility enabled the wetting and activation process dominating the first 50 cycles for the $MnO_2$/pCNT and $MnO_2$/aCNT electrodes, leading to a capacity increase. The $MnO_2$ and $MnO_2$/rCNT electrodes also underwent a wetting and activation process. However, the capacity increase was less significant than the capacity fade, owing to the poor reversibility of the electrodes.

The relationship between the $MnO_2$ content and capacity reversibility was investigated. Most reactive sites on the surface of aCNTs were anchored by $MnO_2$ nanoparticles when the content of $MnO_2$ was 50 wt% in the composite (Fig. S1a). The TGA profiles in Fig. S6 show that it was not feasible to fabricate $MnO_2$/CNT electrodes with $MnO_2$ content higher than 50 wt% even when the fabrication process was extended to 6 days using aCNTs and excess $KMnO_4$. Therefore, $MnO_2$/aCNT electrodes with 30 wt% and 40 wt% $MnO_2$ loading were fabricated to study the dependence of reversibility on the $MnO_2$ content. Figs. S7a and b show the discharge curves of the $MnO_2$/aCNT electrodes with 30 wt% and 40 wt% $MnO_2$ loadings at 0.2 A $g^{-1}$, respectively. $MnO_2$ content had little effect on the reversibility in the first cycle, being 66–70% for the $MnO_2$/aCNT electrodes with $MnO_2$ loading ranging from 30 wt% to 50 wt% (Figs. 5d, S7a, and S7b). Moreover, they shared the same feature of slight capacity increase from the 2nd cycle to the 50th cycle. These results suggested that the $MnO_2$/aCNT electrodes possessed similar capacity reversibility when the $MnO_2$ content was lower than 50 wt %.

The $MnO_2$, $MnO_2$/rCNT, $MnO_2$/pCNT, and $MnO_2$/aCNT electrodes were cycled in the potential window of 0.01–3.00 V at a current density of 0.2 A $g^{-1}$ (Fig. 6a). The $MnO_2$/aCNT electrode delivered discharge capacities of 1043.5/718.3 mA h $g^{-1}$ for the initial and second cycles, respectively. The capacity kept increasing from the 3rd cycle until the 70th cycle, and a maximum of 843.8 mA h $g^{-1}$ was reached. The $MnO_2$/pCNT electrode exhibited 903.8/626.6 mA h $g^{-1}$ in the 1st and 2nd cycle, respectively. Capacity increase from the 3rd cycle was also observed. In comparison, the $MnO_2$/rCNT and $MnO_2$ electrodes exhibited poor performances. The initial capacities of 1203.8 mA h $g^{-1}$ and 616.5 mA h $g^{-1}$ degraded to 380.2 mA h $g^{-1}$ and 145.4 mA h $g^{-1}$ after 20 cycles for the $MnO_2$/rCNT and $MnO_2$ electrodes, respectively. For the $MnO_2$/aCNT electrode, its capacity at the 70th cycle exceeded its theoretical maximum value. The electrode consisted of aCNTs, $MnO_2$, and water in a weight ratio of 42:50:8, as determined by TGA (Fig. S1d). The aCNTs exhibited a capacity of 175.3 mA h $g^{-1}$ at the 70$^{th}$ cycle (Fig. S8), and the theoretical maximum capacity of $MnO_2$ is 1233 mA h $g^{-1}$ [46–48], assuming $Mn^{4+}$ to $Mn^0$. Thus, the upper limit of the discharge capacity of the $MnO_2$/aCNT electrode was 690.1 mA h $g^{-1}$ (i.e. 175.3 mA h $g^{-1}$ × 42 wt% + 1233 mA h $g^{-1}$ × 50 wt% = 690.1 mA h $g^{-1}$), which was 18% lower than the actual capacity (843.8 mA h $g^{-1}$). The excess capacity may have originated from capacitive lithium storage behavior at the $MnO_2$/carbon interface, with the positive charge of $Li^+$ compensated for by electrons in the aCNTs. Such interfacial excess $Li^+$ storage behavior has been reported in a similar system involving the $LiFePO_4$/graphene interface reconstructed by Fe–O–C bonds [49].

Electrochemical impedance spectra (EIS) of the $MnO_2$, $MnO_2$/rCNT, $MnO_2$/pCNT, and $MnO_2$/aCNT electrodes were performed to reveal the impedance change and transport kinetics during cycling. Figs. S9a–d shows the Nyquist plots of these electrodes before and after 50 cycles at 0.2 A $g^{-1}$. The equivalent circuit model is shown in Fig. S9e, and the calculated parameters are listed in Table S1. In the equivalent circuit, $R_\Omega$ corresponds to the Ohmic resistance between the electrode and electrolyte; $R_{ct}$ reflects the charge transfer resistance; $CPE_{dl}$ is related to the non-ideal capacitance of the double layer. Due to the formation of SEI during cycling, $R_{SEI}$ and $CPE_{SEI}$ are added to the equivalent circuit, which represent the resistance and non-ideal capacitance of the SEI layer. The most important parameter, $R_{ct}$, is directly related to reaction kinetics. After 50 cycles, both $MnO_2$/pCNT and $MnO_2$/aCNT electrodes exhibited lower charge-transfer resistances than their initial values, indicating improved Li-reaction kinetics during cycling. This can be attributed to the better contact between electrolyte and active materials during the initial wetting of the electrode and activation process, thereby leading to the capacity increase as shown in Fig. 6a. The $Li^+$ diffusion coefficients were determined by the following equation: $D_{L_i} = \frac{R^2T^2}{2A^2n^4F^4C^2\sigma^2}$ (where $R$ is the gas constant in the ideal gas equation, $T$ is the absolute temperature, $A$ is the surface area of the electrode, $n$ is the number of electrons per molecule during reaction, $F$ is the Faraday constant, $C$ is the concentration of $Li^+$, and $\sigma$ is the Warburg coefficient obtained from the slopes of $Z'$ versus $\omega^{-1/2}$ in the low frequency region as shown in Fig. S9 a-d insets) [11]. After 50 cycles, the diffusion coefficient of the $MnO_2$/aCNT electrode ($2.1 \times 10^{-12}$ cm$^2$ s$^{-1}$) was 60% higher than that of the $MnO_2$/pCNT electrode ($1.3 \times 10^{-12}$ cm$^2$ s$^{-1}$), and was approximately three orders of magnitude higher than those of the $MnO_2$ ($1.9 \times 10^{-15}$ cm$^2$ s$^{-1}$) and $MnO_2$/rCNT ($3.6 \times 10^{-15}$ cm$^2$ s$^{-1}$) electrodes. These results indicated the advantages of $MnO_2$/aCNT electrode in facilitating $Li^+$ diffusion, thus resulting in excellent rate performances.

The rate performances of the $MnO_2$, $MnO_2$/rCNT, $MnO_2$/pCNT, and $MnO_2$/aCNT electrodes at a discharge rate of 0.5 A $g^{-1}$ are shown in Fig. 6b. The $MnO_2$/aCNT electrode exhibited the best rate performance and delivered high reversible discharge capacities of 671.9 mA h $g^{-1}_{electrode}$, 649.1 mA h $g^{-1}_{electrode}$, 619.2 mA h $g^{-1}_{electrode}$, 539.9 mA h $g^{-1}_{electrode}$, and 395.8 mA h $g^{-1}_{electrode}$ at stepwise charge rates of 0.5 A $g^{-1}$, 1 A $g^{-1}$, 2 A $g^{-1}$, 5 A $g^{-1}$, and 10 A $g^{-1}$, respectively. When the charge rate was set back to 0.5 A $g^{-1}$, the electrode resumed a capacity of 648.1 mA h $g^{-1}$. The $MnO_2$/pCNT electrode exhibited inferior rate performances at charge rates of 0.5–2 A $g^{-1}$, with significant capacity collapse at 5 A $g^{-1}$ and 10 A $g^{-1}$. Both the $MnO_2$ and $MnO_2$/rCNT electrodes exhibited very low capacities at 0.5 A $g^{-1}$, and almost failed at higher rates. The inferior rate performances of these electrodes might have been attributed to the aggregation of their active materials due to the absence of Mn–O–C linkage, and their separation from the metal current collector or CNTs at high rates. The rate performance of the $MnO_2$/aCNT electrode was compared with other $MnO_2$/C electrodes reported in the literature, including CNS@$MnO_2$, $MnO_2$/rGO, $MnO_2$@CNT, $MnO_2$/C nanospheres, and rGO-$MnO_2$@CNT (Table 1) [50–54]. The $MnO_2$/aCNT electrode in the present study exhibited the best rate performance. Long-term cycling tests of the $MnO_2$/aCNT electrode were carried out at high charge/discharge rates of 2 A $g^{-1}$ and 5 A $g^{-1}$ (Fig. 6c). The electrode delivered initial capacities of 824.0 mA h $g^{-1}$ and 718.3 mA h $g^{-1}$ at 2 A $g^{-1}$ and 5 A $g^{-1}$, respectively. At 2 A $g^{-1}$, the capacity increased until the 150th cycle, with a maximum of 630.2 mA h $g^{-1}$. The electrode exhibited low capacity fading rates of 0.075% and 0.140% per cycle from the 2nd cycle to the 1000th cycle

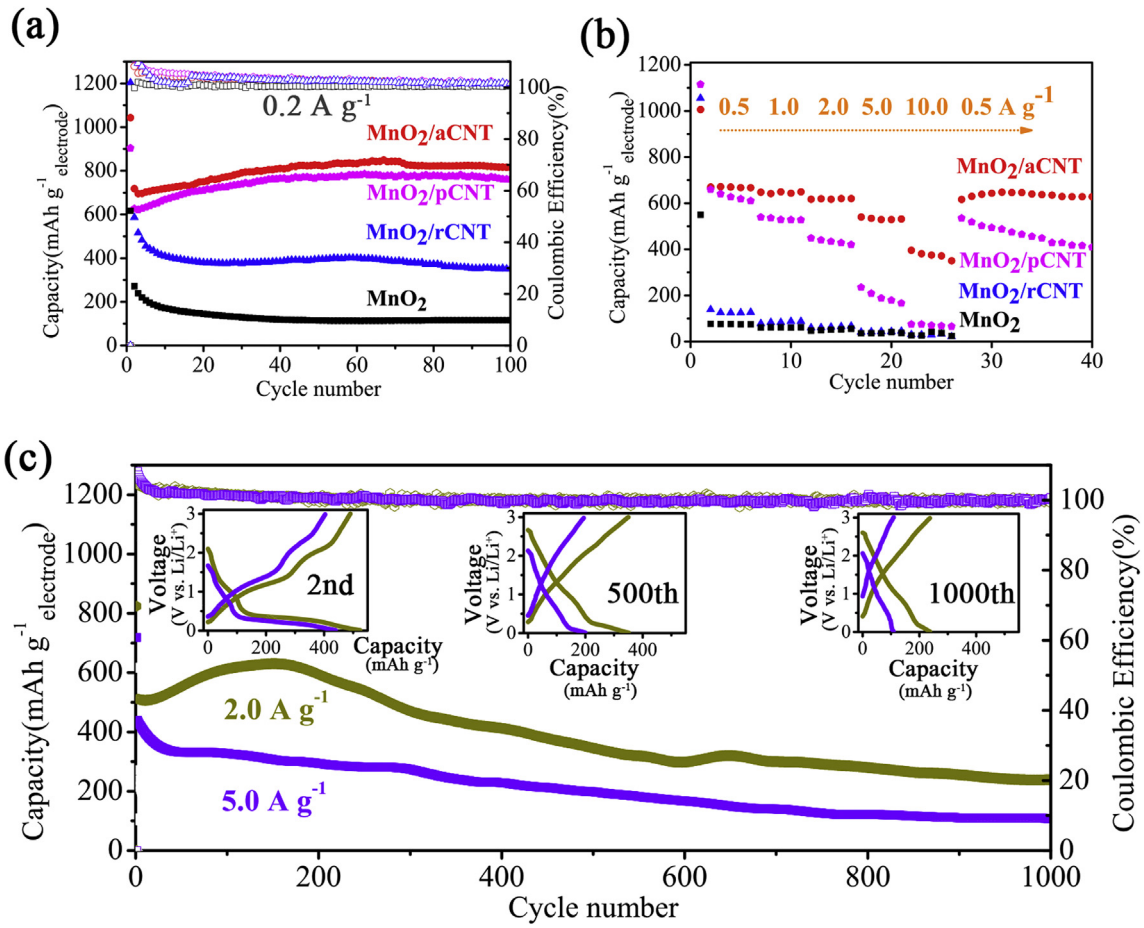


**Fig. 6.** (a) Cycling performance of the $MnO_2$, $MnO_2$/rCNT, $MnO_2$/pCNT, and $MnO_2$/aCNT electrodes at 0.2 A $g^{-1}$. (b) Rate performance at a discharge rate of 0.5 A $g^{-1}$ and stepwise charge rates of 0.5 A $g^{-1}$, 1 A $g^{-1}$, 2 A $g^{-1}$, 5 A $g^{-1}$, and 10 A $g^{-1}$. (c) Long-term cycling performance of the $MnO_2$/aCNT electrode at high charge/discharge rates of 2 A $g^{-1}$ and 5 A $g^{-1}$. (A colour version of this figure can be viewed online.)

**Table 1**
Comparison of the rate performance of the $MnO_2$/aCNT electrode with other $MnO_2$/C electrodes reported in the literature.

| Electrode | Current density (A $g^{-1}$) | Specific capacity (mAh $g^{-1}$) | References |
|---|---|---|---|
| CNS@$MnO_2$ | 1.0 | 225.0 | [50] |
| $MnO_2$/rGO | 6.2 | 400.0 | [51] |
| $MnO_2$@CNT | 2.0 | 250.0 | [52] |
| $MnO_2$/C nanospheres | 1.0 | 540.0 | [53] |
| rGO-$MnO_2$@CNT | 2.0 | 480.6 | [54] |
| $MnO_2$/aCNT | 5.0 and 10.0 | 539.9 and 395.8 | this study |

at 2 A $g^{-1}$ and 5 A $g^{-1}$, respectively.

SEM and TEM images of the $MnO_2$/aCNT electrode after 100 cycles at 2 A $g^{-1}$ are shown in Fig. S10. $MnO_2$ aggregation was not observed in the cycled electrode and the diameter of the aCNT bundles increased due to the formation of SEI (Fig. S10a). $MnO_2$ nanoparticles were still tightly anchored on the CNTs, indicating the stability of the electrode structure after rapid charge/discharge processes (Fig. S10b). The structural stability of the $MnO_2$/aCNT electrode was ascribed to the strong chemical interaction between the $MnO_2$ particles and aCNT framework by Mn–O–C bonds. The presence of the Mn–O–C linkage during charge/discharge processes was confirmed by O 1s XPS spectra of the $MnO_2$/aCNT electrode after 100 cycles at 2 A $g^{-1}$ (Fig. S11). Note that the intensity of the C–O/C=O type species increased compared to the electrode before cycling due to the deposition of an organic layer related to the formation of SEI.

The ultrahigh rate performance and long-term cycling stability of the $MnO_2$/aCNT electrode were ascribed to the electrode structure. Specifically, (1) the $MnO_2$ nanoparticles allowed a large fraction of surface atoms to contact with the electrolyte, and provided short diffusion pathways for rapid $Li^+$ diffusion; (2) the free-standing aCNT scaffold provided 3D continuous electron pathways, which allowed efficient electron transfer and the alleviation of polarization; (3) the robust contact between the $MnO_2$ and aCNTs by the Mn–O–C linkage enabled the flexible aCNT network to accommodate the strain of the electrode, and prevented separation of the active materials from the aCNT framework during the rapid charge/discharge processes.

The high rate performance of the $MnO_2$/aCNT electrode was also associated with the capacitive mechanism. The changes in the capacitive lithium storage behavior during long-term cycling were identified from discharge/charge voltage profiles (Fig. 6c inset). At the 2nd cycle, several discharge/charge plateaus were observed, which corresponded to battery-type diffusion processes. At the 500th cycle, only one discharge plateau was observed. At the 1000th cycle, there was no discharge plateau, and the linear galvanostatic discharge/charge profiles suggested a dominant capacitive contribution to the charge storage. These results demonstrated that the capacitive lithium storage behavior gradually evolved during long-term cycling.

The capacitive contribution to lithium storage of the $MnO_2$/aCNT electrode was further quantified by CV measurements at various scan rates between 0.2 mV $s^{-1}$ and 20 mV $s^{-1}$ (Fig. 7a). A power law relationship between the current response ($i$) and scan rate ($v$) can be used to identify the storage mechanism: $i = av^b$, where $a$ and $b$ are adjustable parameters. When $b$ equals 1, the response current is proportional to the scan rate, indicating a capacitive process. When $b$ equals 0.5, the response current satisfies Cottrell's equation, reflecting a diffusion-controlled process [3,55]. The $b$ value can be obtained from the slope of the log $i$ versus log $v$ plot (Fig. 7b). The $b$ values were 0.77, 0.72, 0.85, and 0.85 at 1.6 V, 2.0 V, 2.4 V, and 2.8 V in the charge process, and 0.87, 0.87, 0.77, and 0.85 at 0.5 V, 1.0 V, 1.5 V, and 2.0 V in the discharge process. The $b$ values between 0.5 and 1.0 implied that the lithium storage process was a hybrid of the semi-infinite diffusion process and the capacitive surface mechanism. The current response $i$ at each potential can be separated into the capacitive current ($k_1v$) and diffusion current ($k_2v^{1/2}$): $i(V) = k_1v + k_2v^{1/2}$ [56]. The values of $k_1$ and $k_2$ can be determined from the slope and intercept of $i/v^{1/2}$ versus $v^{1/2}$ plot. The shaded area in Fig. 7c shows the capacitive current in comparison with the total current at 20 mV $s^{-1}$. The capacitance contribution (460 C $g^{-1}$) accounted for 65.6% of the total capacity (700 C $g^{-1}$), suggesting that the $MnO_2$/aCNT electrode was mainly controlled by the capacitive behavior at a fast scan rate of 20 mV $s^{-1}$. By subtracting the surface-controlled capacity from the total capacity, the diffusion-controlled process contributed only 240 C $g^{-1}$ to the capacity. The capacitance contribution percentage would be smaller than 65.6% at lower scan rates. CV measurements of the aCNT electrode were also conducted at scan rates between 0.2 mV $s^{-1}$ and 20 mV $s^{-1}$, and the capacitance contribution of aCNTs was only 70.5 C $g^{-1}$ at 20 mV $s^{-1}$ (Fig. S12), compared to 460 C $g^{-1}$ for the $MnO_2$/aCNT electrode. Therefore, the dominant capacitive contribution of the $MnO_2$/aCNT electrode originated from $MnO_2$ particles instead of aCNTs.

The capacity contribution could also be quantified from the valence state change of manganese, by measuring the separation between the two main peaks in the Mn 3s spectrum [57]. The Mn 3s XPS binding energy region of the $MnO_2$/aCNT electrode was characterized in the fully charged state (3.0 V) and fully discharged state (0.01 V). The separations of the two main peaks were 5.83 eV and 6.25 eV at 3.0 V and 0.01 V, which corresponded to Mn valences of 2.4 and 2.0, respectively (Fig. 7d). According to Faraday's law, Mn delivered 700 C $g^{-1}$ in the diffusion-controlled process ($\frac{(2.4-2.0)\times 9.65\times 10^4\ C\ mol^{-1}}{55\ g\ mol^{-1}} = 700\ C\ g^{-1}$). Given that Mn accounted for 31.6 wt% in the $MnO_2$/aCNT composites (55/87 × 50 wt% = 31.6 wt %), a capacity of 222 C $g^{-1}$ originated from the redox reaction of manganese (700 C $g^{-1}$ × 31.6 wt% = 222 C $g^{-1}$). This result was in agreement with the kinetic analysis (i.e. 240 C $g^{-1}$ from the diffusion-controlled process).

The $MnO_2$/aCNT electrode exhibited a hybrid behavior of a supercapacitor and battery and outstanding electrochemical performance at ultrahigh current densities. A possible lithium storage mechanism is proposed. The battery behavior arises from semi-infinite $Li^+$ diffusion, accompanied by the redox reaction of manganese. The capacitive behavior originates from excess $Li^+$ storage at the $MnO_2$/aCNT interface, and the positive charge can be compensated for by the extra electrons on the surface of the aCNTs. The capacitive process is responsible for instantaneous charge transfer. Since the capacitive process is the dominating component to the total capacity at ultrahigh current densities, large amounts of energy can be rapidly delivered or stored in the $MnO_2$/aCNT electrode. This result makes the anode design promising for hybrid supercapacitor-battery energy storage applications.

## 4. Conclusion

A free-standing $MnO_2$/aCNT electrode was fabricated and applied in a hybrid supercapacitor-battery energy storage device. $MnO_2$ nanoparticles were uniformly attached to the surface of aCNTs through Mn–O–C linkages. The aCNT network was highly

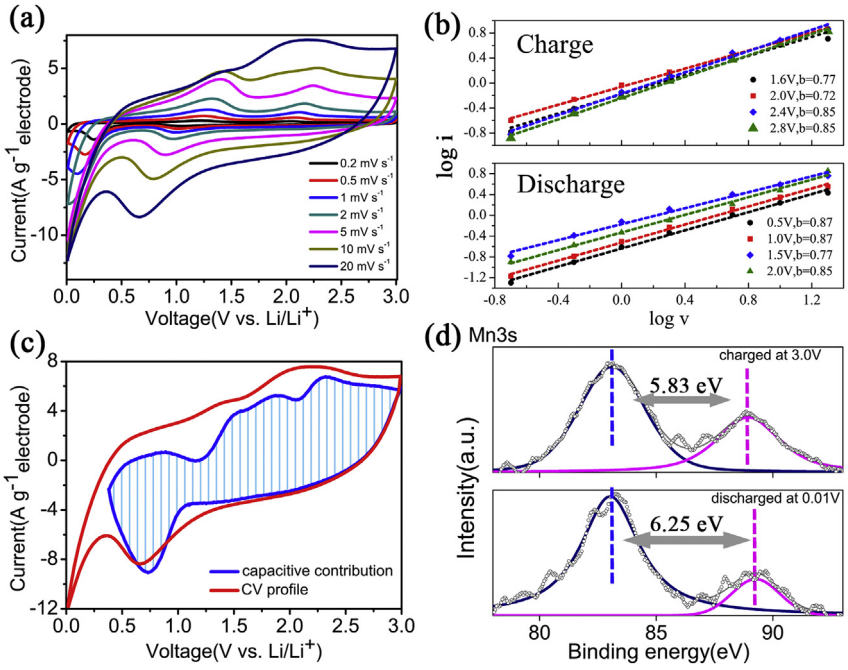


**Fig. 7.** Kinetic analysis of the $MnO_2$/aCNT electrode. (a) CV profiles at different scan rates between 0.2 mV $s^{-1}$ to 20 mV $s^{-1}$. (b) Determination of $b$-values at different potentials. (c) CV profile at 20 mV $s^{-1}$. The shaded area represents the capacitive charge storage contribution. (d) XPS spectra of the Mn 3s region at the fully charged state (3.0 V) and fully discharged state (0.01 V). (A colour version of this figure can be viewed online.)

elastic and conductive. This network served as a conductive scaffold and buffered the volume change of $MnO_2$ during the rapid charge/discharge processes. The presence of $MnO_2$ nanoparticles facilitated the rapid diffusion of lithium ions and interfacial capacitive lithium storage. The $MnO_2$/aCNT electrode exhibited a reversible capacity higher than its theoretical maximum value at 0.2 A $g^{-1}$, owing to the capacitive lithium storage behavior. The lithium storage of the electrode was a surface-dominated capacitive process. The $MnO_2$/aCNT electrode exhibited outstanding high-current performance (395.8 mA h $g^{-1}$ at 10 A $g^{-1}$, 630.2 mA h $g^{-1}$ after 150 cycles at 2 A $g^{-1}$) and low capacity fading rates (0.075% and 0.140% per cycle over 1000 cycles at 2 A $g^{-1}$ and 5 A $g^{-1}$). These results hint at the potential of the $MnO_2$/aCNT structure in high-performance hybrid supercapacitor-battery energy storage systems.

## Acknowledgements

This study was supported by NSFC (Grant No. 51472141) and the National Key Research and Development Program of China (Grant No. 2017YFA0205800). JL acknowledges support by NSF ECCS-1610806.

## Appendix A. Supplementary data

Supplementary data related to this article can be found at https://doi.org/10.1016/j.carbon.2018.06.046.

## References

[1] H. Wang, C. Zhu, D. Chao, Q. Yan, H.J. Fan, Nonaqueous hybrid lithium-ion and sodium-ion capacitors, Adv. Mater. 29 (46) (2017). UNSP 1702093.
[2] P. Simon, Y. Gogotsi, Materials for electrochemical capacitors, Nat. Mater. 7 (11) (2008) 845–854.
[3] P. Simon, Y. Gogotsi, B. Dunn, Materials science. Where do batteries end and supercapacitors begin? Science 343 (6176) (2014) 1210–1211.
[4] Y. Li, B. Tan, Y. Wu, Mesoporous $Co_3O_4$ nanowire arrays for lithium ion batteries with high capacity and rate capability, Nano Lett. 8 (1) (2008) 265–270.
[5] O. Rhee, G. Lee, J. Choi, Highly ordered $TiO_2$ microcones with high rate performance for enhanced lithium-ion storage, ACS Appl. Mater. Interfaces 8 (23) (2016) 14558–14563.
[6] H. Duan, J. Gnanaraj, X. Chen, B. Li, J. Liang, Fabrication and characterization of $Fe_3O_4$-based Cu nanostructured electrode for Li-ion battery, J. Power Sources 185 (1) (2008) 512–518.
[7] Y.J. Mai, D. Zhang, Y.Q. Qiao, C.D. Gu, X.L. Wang, J.P. Tu, MnO/reduced graphene oxide sheet hybrid as an anode for Li-ion batteries with enhanced lithium storage performance, J. Power Sources 216 (2012) 201–207.
[8] H. Xia, M. Lai, L. Lu, Nanoflaky $MnO_2$/carbon nanotube nanocomposites as anode materials for lithium-ion batteries, J. Mater. Chem. 20 (33) (2010) 6896.
[9] H. Wang, L.-F. Cui, Y. Yang, H.S. Casalongue, J.T. Robinson, Y. Liang, et al., $Mn_3O_4$-graphene Hybrid as a High Capacity Anode Material for Lithium Ion Batteries, 2010 arXiv preprint arXiv:10093923.
[10] W. Zhang, J. Li, J. Zhang, J. Sheng, T. He, M. Tian, et al., Top-down strategy to synthesize mesoporous dual carbon armored MnO nanoparticles for lithium-ion battery anodes, ACS Appl. Mater. Interfaces 9 (14) (2017) 12680–12686.
[11] J. Zhang, W. Zhang, T. He, I.S. Amiinu, Z. Kou, J. Li, et al., Smart reconstruction of dual-carbon decorated MnO for anode with high-capacity and ultralong-life lithium storage properties, Carbon 115 (2017) 95–104.
[12] W. Zhang, J. Sheng, J. Zhang, T. He, L. Hu, R. Wang, et al., Hierarchical three-dimensional MnO nanorods/carbon anodes for ultralong-life lithium-ion batteries, J. Mater. Chem. 4 (43) (2016) 16936–16945.
[13] Y. Dou, L. Zhang, X. Xu, Z. Sun, T. Liao, S.X. Dou, Atomically thin non-layered nanomaterials for energy storage and conversion, Chem. Soc. Rev. 46 (23) (2017) 7338–7373.
[14] J. Zhang, T. He, W. Zhang, J. Sheng, I.S. Amiinu, Z. Kou, et al., Na-Mn-O nanocrystals as a high capacity and long life anode material for Li-ion batteries, Adv. Energy Mater. 7 (5) (2017) 1602092.
[15] T. Wei, M. Zhang, P. Wu, Y.-J. Tang, S.-L. Li, F.-C. Shen, et al., POM-based metal-organic framework/reduced graphene oxide nanocomposites with hybrid behavior of battery-supercapacitor for superior lithium storage, Nanomater. Energy 34 (2017) 205–214.
[16] A.S. Aricò, P. Bruce, B. Scrosati, J.M. Tarascon, W.V. Schalkwijk, Nanostructured materials for advanced energy conversion and storage devices, Nat. Mater. 4 (5) (2005) 366.
[17] X. Rui, Z. Lu, H. Yu, D. Yang, H.H. Hng, T.M. Lim, et al., Ultrathin $V_2O_5$ nanosheet cathodes: realizing ultrafast reversible lithium storage, Nanoscale 5 (2) (2013) 556–560.
[18] K. Shiva, H.S.S. Ramakrishna Matte, H.B. Rajendra, A.J. Bhattacharyya, C.N.R. Rao, Employing synergistic interactions between few-layer $WS_2$ and reduced graphene oxide to improve lithium storage, cyclability and rate capability of Li-ion batteries, Nanomater. Energy 2 (5) (2013) 787–793.
[19] M. Sathiya, A.S. Prakash, K. Ramesha, J.M. Tarascon, A.K. Shukla, $V_2O_5$-anchored carbon nanotubes for enhanced electrochemical energy storage, J. Am. Chem. Soc. 133 (40) (2011) 16291–16299.
[20] T. Yuan, Y. Jiang, W. Sun, B. Xiang, Y. Li, M. Yan, et al., Ever-increasing pseudocapacitance in RGO-MnO-RGO sandwich nanostructures for ultrahigh-rate lithium storage, Adv. Funct. Mater. 26 (13) (2016) 2198–2206.
[21] L.L. Tian, M.J. Zhang, C. Wu, Y. Wei, J.X. Zheng, L.P. Lin, et al., γ-$Fe_2O_3$ nanocrystalline microspheres with hybrid behavior of battery-supercapacitor for superior lithium storage, ACS Appl. Mater. Interfaces 7 (47) (2015) 26284–26290.
[22] Y. Shi, X. Zhou, G. Yu, Material and structural design of novel binder systems for high-energy, high-power lithium-ion batteries, Acc. Chem. Res. 50 (11) (2017) 2642–2652.
[23] K. Shiva, H.B. Rajendra, K.S. Subrahmanyam, A.J. Bhattacharyya, C.N. Rao, Improved lithium cyclability and storage in mesoporous $SnO_2$ electronically wired with very low concentrations (</=1 %) of reduced graphene oxide, Chemistry 18 (15) (2012) 4489–4494.
[24] S.L. Chou, Y. Pan, J.Z. Wang, H.K. Liu, S.X. Dou, Small things make a big difference: binder effects on the performance of Li and Na batteries, Phys. Chem. Chem. Phys. 16 (38) (2014) 20347–20359.
[25] R. Wang, L. Feng, W. Yang, Y. Zhang, Y. Zhang, W. Bai, et al., Effect of different binders on the electrochemical performance of metal oxide anode for lithium-ion batteries, Nanoscale Res. Lett. 12 (1) (2017) 575.
[26] Y. Wu, J. Wang, K. Jiang, S. Fan, Applications of carbon nanotubes in high performance lithium ion batteries, Front. Phys. 9 (3) (2013) 351–369.
[27] K. Jiang, Q. Li, S. Fan, Nanotechnology: spinning continuous carbon nanotube yarns, Nature 419 (6909) (2002) 801.
[28] X. He, Y. Wu, F. Zhao, J. Wang, K. Jiang, S. Fan, Enhanced rate capabilities of $Co_3O_4$/carbon nanotube anodes for lithium ion battery applications, J. Mater. Chem. 1 (37) (2013) 11121.
[29] S. Luo, H. Wu, Y. Wu, K. Jiang, J. Wang, S. Fan, $Mn_3O_4$ nanoparticles anchored on continuous carbon nanotube network as superior anodes for lithium ion batteries, J. Power Sources 249 (2014) 463–469.
[30] Y. Wu, Y. Wei, J. Wang, K. Jiang, S. Fan, Conformal $Fe_3O_4$ sheath on aligned carbon nanotube scaffolds as high-performance anodes for lithium ion batteries, Nano Lett. 13 (2) (2013) 818–823.
[31] T. Brousse, D. Belanger, J.W. Long, To be or not to be pseudocapacitive? J. Electrochem. Soc. 162 (5) (2015) A5185–A5189.
[32] D. Wang, K. Wang, H. Wu, Y. Luo, L. Sun, Y. Zhao, et al., $CO_2$ oxidation of carbon nanotubes for lithium-sulfur batteries with improved electrochemical performance, Carbon 132 (2018) 370–379.
[33] S. Luo, Y. Luo, H. Wu, M. Li, L. Yan, K. Jiang, et al., Self-assembly of 3D carbon nanotube sponges: a simple and controllable way to build macroscopic and ultralight porous architectures, Adv. Mater. 29 (1) (2017).
[34] P. Slobodian, P. Riha, R. Olejnik, U. Cvelbar, P. Saha, Enhancing effect of $KMnO_4$ oxidation of carbon nanotubes network embedded in elastic polyurethane on overall electro-mechanical properties of composite, Compos. Sci. Technol. 81 (2013) 54–60.
[35] J.E. Post, D.R. Veblen, Crystal structure determinations of synthetic sodium, magnesium, and potassium birnessite using TEM and the Rietveld method, Am. Mineral. 75 (5–6) (1990) 477–489.
[36] X. Liang, C. Hart, Q. Pang, A. Garsuch, T. Weiss, L.F. Nazar, A highly efficient polysulfide mediator for lithium-sulfur batteries, Nat. Commun. 6 (2015) 5682.
[37] X. Xie, L. Gao, Characterization of a manganese dioxide/carbon nanotube composite fabricated using an in situ coating method, Carbon 45 (12) (2007) 2365–2373.
[38] C. Julien, Raman spectra of birnessite manganese dioxides, Solid State Ionics 159 (3–4) (2003) 345–356.
[39] J.S. Oh, K.H. Ahn, J.S. Hong, Dispersion of entangled carbon nanotube by melt extrusion, Korea Aust. Rheol. J. 22 (2) (2010) 89–94.
[40] A.S. Ivanova, G.S. Litvak, V.V. Mokrinskii, L.M. Plyasova, V.I. Zaikovskii, V.V. Kaichev, et al., The influence of the active component and support nature, gas mixture composition on physicochemical and catalytic properties of catalysts for soot oxidation, J. Mol. Catal. Chem. 310 (1–2) (2009) 101–112.
[41] S. Hussain, R. Amade, E. Jover, E. Bertran, Water plasma functionalized CNTs/$MnO_2$ composites for supercapacitors, Sci. World J. 2013 (2013) 832581.
[42] G. Zhou, D.W. Wang, L.C. Yin, N. Li, F. Li, H.M. Cheng, Oxygen bridges between NiO nanosheets and graphene for improvement of lithium storage, ACS Nano 6 (4) (2012) 3214.
[43] J. Wang, H. Tang, L. Zhang, H. Ren, R. Yu, Q. Jin, et al., Multi-shelled metal oxides prepared via an anion-adsorption mechanism for lithium-ion batteries, Nat. Energy 1 (5) (2016) 16050.
[44] S.J. An, J. Li, C. Daniel, D. Mohanty, S. Nagpure, D.L. Wood, The state of understanding of the lithium-ion-battery graphite solid electrolyte interphase (SEI) and its relationship to formation cycling, Carbon 105 (2016) 52–76.
[45] Y. Matsumura, S. Wang, J. Mondori, Mechanism leading to irreversible capacity loss in Li ion rechargeable batteries, J. Electrochem. Soc. 142 (9) (1995) 2914–2918.
[46] Y. Abu-Lebdeh, I. Davidson, Nanotechnology for Lithium-ion Batteries, Springer US, 2013.

[47] B. Sun, Z. Chen, H.S. Kim, H. Ahn, G. Wang, MnO/C core–shell nanorods as high capacity anode materials for lithium-ion batteries, J. Power Sources 196 (6) (2011) 3346–3349.
[48] H.R. Byon, B.M. Gallant, S.W. Lee, Y. Shao-Horn, Role of oxygen functional groups in carbon nanotube/graphene freestanding electrodes for high performance lithium batteries, Adv. Funct. Mater. 23 (8) (2013) 1037–1045.
[49] Y. Duan, B. Zhang, J. Zheng, J. Hu, J. Wen, D.J. Miller, et al., Excess Li-Ion storage on reconstructed surfaces of nanocrystals to boost battery performance, Nano Lett. 17 (10) (2017) 6018–6026.
[50] J. Yue, X. Gu, L. Chen, N. Wang, X. Jiang, H. Xu, et al., General synthesis of hollow $MnO_2$, $Mn_3O_4$ and MnO nanospheres as superior anode materials for lithium ion batteries, J. Mater. Chem. 2 (41) (2014) 17421–17426.
[51] S.J. Kim, Y.J. Yun, K.W. Kim, C. Chae, S. Jeong, Y. Kang, et al., Superior lithium storage performance using sequentially stacked $MnO_2$/reduced graphene oxide composite electrodes, ChemSusChem. 8 (8) (2015) 1484–1491.
[52] W. Mao, G. Ai, Y. Dai, Y. Fu, Y. Ma, S. Shi, et al., In-situ synthesis of $MnO_2$@CNT microsphere composites with enhanced electrochemical performances for lithium-ion batteries, J. Power Sources 310 (2016) 54–60.
[53] S.-Z. Huang, Y. Cai, J. Jin, J. Liu, Y. Li, H.-E. Wang, et al., Unique walnut-shaped porous $MnO_2$/C nanospheres with enhanced reaction kinetics for lithium storage with high capacity and superior rate capability, J. Mater. Chem. 4 (11) (2016) 4264–4272.
[54] Y. Li, D. Ye, B. Shi, W. Liu, R. Guo, H. Pei, et al., Free-standing reduced graphene oxide/$MnO_2$-reduced graphene oxide-carbon nanotube nanocomposite flexible membrane as an anode for improving lithium-ion batteries, Phys. Chem. Chem. Phys. 19 (11) (2017) 7498–7505.
[55] M.R. Lukatskaya, B. Dunn, Y. Gogotsi, Multidimensional materials and device architectures for future hybrid energy storage, Nat. Commun. 7 (2016) 12647.
[56] T.C. Liu, Behavior of molybdenum nitrides as materials for electrochemical capacitors, J. Electrochem. Soc. 145 (6) (1998) 1882–1888.
[57] V.R. Galakhov, M. Demeter, S. Bartkowski, M. Neumann, N.A. Ovechkina, E.Z. Kurmaev, et al., Mn 3s exchange splitting in mixed-valence manganites, Phys. Rev. B 65 (11) (2002).